UC Berkeley
UC Berkeley Previously Published Works

Title
Nanocomposites Based on Coil-Comb Diblock Copolymers

Permalink
https://escholarship.org/uc/item/5bv6j1zf

Journal
Macromolecules, 54(2)

ISSN
0024-9297

Authors
Huang, Jingyu
Hall, Aaron
Jayapurna, Ivan
et al.

Publication Date
2021-01-26

DOI
10.1021/acs.macromol.0c02441

Supplemental Material
https://escholarship.org/uc/item/5bv6j1zf#supplemental

Peer reviewed

eScholarship.org Powered by the California Digital Library
University of California

Nanocomposites Based on Coil-Comb Diblock Copolymers

Jingyu Huang,[†,‖] Aaron Hall,[†,‖] Ivan Jayapurna,[†] Samana Algharbi[†], Valeriy Ginzburg[⊥], and Ting Xu[*,†,‡,§]

[†] Department of Materials Science & Engineering, University of California, Berkeley, California 94720, United States

[‡] Materials Science Division, Lawrence Berkeley National Laboratory, Berkeley, California 94720, United States

[§] Department of Chemistry, University of California, Berkeley, California 94720, United States

⊥ Core R&D, The Dow Chemical Company, Midland, Michigan 48674, United States

[‖] Authors contributed equally

[*] Email: tingxu@berkeley.edu

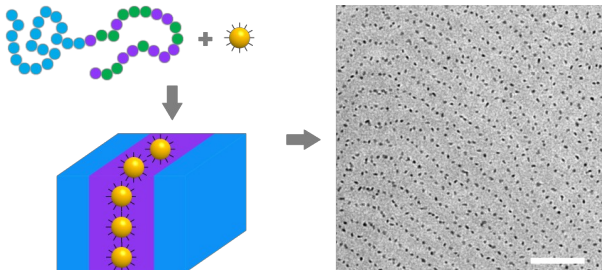

ABSTRACT. Polymer chain architecture is an important factor determining the phase behavior of nanoparticle (NP) assembly in polymer matrices. Block copolymers (BCPs) containing a random copolymer (RCP) block present a convenient variation on traditional BCPs to tune the interaction parameters between the polymer blocks and the nanofillers as well as to evaluate the effect of chain architecture on the NP arrangements within BCP microdomains. Here, we synthesized BCPs with a coil polystyrene (PS) block and a comb RCP block through reversible addition-fragmentation chain transfer polymerization. The RCP block consists of methyl- and

lauryl acrylates, the latter which confers a long-chain alkyl moiety to favorably interact with alkyl-passivated NPs. BCPs showing lamellar, cylindrical, and mixed morphologies were obtained by varying the volume fractions of the RCP block (f_{RCP}). In comparison to coil-coil BCP, the coil-comb BCPs show highly asymmetric phase behavior with respect to f_{RCP}, where lamellar morphologies were observed at f_{RCP} from 0.31 to 0.51. NPs in the size of 4-5 nm were successfully incorporated in the RCP block of the BCPs with periodicities of 30-60 nm. An order-to-order phase transition from lamellae to PS cylinders was observed after the addition of only 1-2 vol% of 5 nm NPs into the BCP with a periodicity of 25 nm and f_{RCP} of 0.51. Self-consistent field theory-density functional theory simulations qualitatively described the observed morphologies and phase transitions in the nanocomposites. The current study presents a platform to fabricate nanocomposites with NP assemblies in coil-comb BCPs that contain a random copolymer block, and provides insight into how polymer chain architecture can affect the phase behavior of BCPs and nanocomposites.

KEYWORDS. coil-comb block copolymer, nanocomposite, self-assembly, chain architecture

INTRODUCTION

Nanoparticle (NP) assembly in block copolymers (BCPs) provides a facile approach to fabricating functional nanocomposite materials with targeted collective properties derived from the building blocks. In order to selectively incorporate NPs into one of the domains, either the NP surface or the polymer should be engineered to generate favorable enthalpic interactions, such as Van der Waals[1, 2] or hydrogen bonding[3, 4], between the NP ligand and the polymer. The entropic contribution upon NP incorporation affects the distribution of NPs in the polymer matrix.[1, 5] Polymer chain architecture is an important parameter in determining polymer conformational entropy, which influences the assembly of NPs in BCP matrices.[6] The compatibility between NPs and polymers is sensitive to the chain architecture, where BCPs with the same chemical compositions but different chain architectures yield varying results due to the varying contributions from chain conformational entropy after NP incorporation.[7] BCPs with chain architectures of coil-coil[1, 8], bottlebrush[9, 10], and coil-comb[11, 12] have all been successfully utilized with NPs to assemble hierarchically structured nanocomposites.

3D NP assemblies in BCP-based coil-comb supramolecular systems have been extensively investigated in our previous studies with a large variety of well-ordered morphologies available.[11, 13] The addition of small molecules in the system facilitates NP incorporation[11] and accelerates the assembly kinetics[14]. However, hydrogen-bonded small molecules can possess instability issues over time, especially in thin films. To overcome this problem, coil-comb diblock copolymers with covalently bonded long alkyl side chains can be designed as a more stable analogue to the supramolecular system for the fabrication of stable nanocomposites. The density of the long alkyl side chains should be tailored to balance the favorable enthalpic interactions to the NP surface chemistry, and the backbone flexibility to

accommodate NPs for the optimization of NP assembly. The comb block can be designed as a random copolymer (RCP) consisting of monomers with different alkyl lengths. The steric repulsion between the alkyl side chains in the comb block can impose bending rigidity to the backbone, leading to the polymer adopting an extended conformation like that seen in bottlebrush polymers.[15] Brush-like polymers show low entanglement, which facilitates fast assembly kinetics.[16] Copolymer sequence and chemical heterogeneity also affect the effective interactions between the NPs and the degree of their spatial dispersion in copolymer melts.[19, 20] Therefore the block-random copolymer architecture presents a versatile platform to tune the physical properties and interactions between the building blocks through the composition in the random block, and the relative molecular weights of the two blocks.[21]

Here, we report the design and synthesis of a coil-comb BCP for the assembly of NPs. BCPs, with a polystyrene (PS) block and a random copolymer (RCP) block containing methyl-, lauryl-, and oligo (ethylene glycol) methyl ether acrylate monomers, were synthesized using reversible addition-fragmentation chain transfer (RAFT) polymerization. The phase behavior of these BCPs was studied as a function of molecular weight of the polymer and the volume fraction of the RCP block (f_{RCP}). NP assembly was investigated as a function of BCP morphology and particle loading. Alkyl-passivated NPs were successfully accommodated in the RCP block due to the favorable enthalpic interactions. An order-to-order morphological transition from lamellae to PS cylinders was observed after the addition of 1-2 vol% of NPs, where the effective f_{RCP} in the nanocomposite is ~0.53. Self-consistent field theory-density functional theory (SCFT-DFT) modeling suggests the transition is driven by the strong preference of the particles towards the RCP block; the effective volume fraction of the PS block is thus reduced and eventually drops below the effective lamellar-hexagonal boundary. These results demonstrate distinct phase

behavior in the coil-comb BCPs and nanocomposites, and indicate the effects of polymer chain architecture on the NP assembly in nanocomposites.

MATERIALS AND METHODS

Materials. 5 nm ZrO_2 NPs coated with 8 carbon alkyl ligands were purchased from Pixelligent. 4 nm Au NPs coated with 18 carbon alkyl ligands (oleylamine) were synthesized according to a previously reported method.[22] All of the NPs were dispersed in toluene at a concentration of 20 mg/mL before use. Polymerization reagents and solvents of the highest purity were purchased from Sigma Aldrich unless otherwise noted. Azobisisobutyronitrile (AIBN) was recrystallized from ethanol prior to use. To remove polymerization inhibitors, methyl acrylate (MA) (99%) and styrene (STY) (98%) were cryodistilled, lauryl acrylate (LA) (90%) was dissolved in hexane, washed 3x with 2M NaOH (Fisher), dried using magnesium sulfate, evaporated under reduced pressure, then passed over a column of basic alumina.[23] Oligo (ethylene glycol) methyl ether acrylate (M_n = 480 Da) (OEGA) was passed over a column of basic alumina. RAFT agents cyanomethyl dodecyl trithiocarbonate and 2-(dodecylthiocarbonothioylthio)-2-methylpropionic acid, 1,3,5-trioxane (TCI), and solvents (ACS Grade: methanol, isopropanol, toluene. HPLC: dichloromethane, pentane) were used as received.

Synthesis of BCPs. Polymerization solutions were prepared by mixing the purified monomers, AIBN, RAFT agent (or macro-RAFT agents for BCP extensions), trioxane (internal NMR standard), and solvents in 20 mL glass ampules. These solutions were subjected to 4 freeze-pump-thaw cycles before the ampules were sealed at 30 mtorr. The polymerizations were held in a 70 ˚C oven until the samples reached high viscosity (typically 12-24 hours). The

ampules were then removed from the oven, cooled in liquid nitrogen, and cracked open. The polymers were precipitated by dropwise addition of the reacted mixture into rapidly stirring anti-solvent (RCP: methanol, PS: methanol or pentane, BCP: methanol or isopropanol). The polymers exhibit drastically varying behavior upon precipitation based on their monomer composition. The PS precipitates as fine powder, while the RCP is a viscous gel. Successfully extended BCPs form powders with a slight tackiness that increases with the RCP fraction. The powders (PS, BCP) were isolated from the anti-solvent using vacuum filtration over a fritted glass filter, washed with ~100 mL more of anti-solvent, then transferred to a glass vial. For the RCP, the anti-solvent was decanted, then the precipitate was dissolved in minimal dichloromethane, transferred to a vial, and the dichloromethane removed by a gentle stream of nitrogen gas. All samples were then dried under vacuum overnight.

Polymer Characterization. Pre-polymerization, post polymerization, and precipitated NMR samples were taken for each polymer. ^{1}H NMR spectra were carried with a Bruker Avance 400 spectrometer (400 MHz) using a 5 mm Z-gradient BBO probe or a Bruker Avance AV 500 spectrometer (500 MHz) using a Z-gradient Triple Broad Band Inverse detection probe. Global monomer conversion was measured on crude reaction mixtures in $CDCl_3$, using trioxane as an internal standard. Number-average (M_n) and weight-average (Mw) molar mass and dispersity (Đ = M_w/M_n) of copolymers were obtained from gel permeation chromatography (GPC) carried out using an Agilent 1260 Infinity series instrument outfitted with 2 300 x 7.5 mm columns (1 Agilent PolyPore column, 1 Agilent Resipore column, in series). THF was used as eluent at 1 mL/min. PS and PMMA standards were used to calibrate the GPC system. Analyte samples at 2

mg/mL were filtered through 0.2 μm polytetrafluoroethylene (PTFE) membranes (VWR) before injection (20 μL).

Sample preparation. A bulk sample was prepared by adding 200 μL of BCP toluene solution or BCP/NP mixture toluene solution into a 1 mL PTFE (Teflon) beaker. The beaker was covered with a glass slide and left in a fume hood to let the solvent evaporate slowly over two days. The sample was then dried under vacuum for 2 hours to remove any trace amount of solvent residue and followed by thermal annealing at 150 ºC in a vacuum oven for 2 days. After annealing, the sample was cooled down naturally to room temperature under vacuum. Thin sectioning of the bulk samples was performed on a Leica EM FC6 cryo-ultramicrotome at -160 ºC. Thin sections were picked up using saturated sucrose solution in phosphate buffer at pH 7.4 and then transferred to 200-mesh TEM grids followed by DI water rinsing to get rid of sucrose.

Transmission Electron Microscope (TEM). Sample imaging was performed on a FEI Tecnai 12 electron microscopy with an accelerating voltage of 120 kV. BCP samples on TEM grids were placed under RuO_4 vapor for 15 min to stain the PS domain. Nanocomposite samples with ZrO_2 NPs were not stained with RuO_4 since we found the staining agent can degrade ZrO_2 NPs and make it impossible to distinguish the BCP morphologies.

Small-angle X-ray Scattering (SAXS). Static SAXS measurements of the bulk samples were performed at Advanced Photon Source 8-ID-E in Argonne National Lab with a 1.240 Å (10 keV) X-ray source. *In situ* SAXS measurements were performed at the synchrotron beamline Advanced Light Source 7.3.3 in Lawrence Berkeley National Lab with a 1.14 Å (10.9 keV) X-ray source. The *in situ* SAXS samples were heated directly from room temperature to 90 ˚C at a heating rate of 10 ˚C/min. Then, the samples were further heated from 90 ˚C to 180 ˚C at an

interval of 10 °C. SAXS profiles were taken after the samples were kept at each temperature for 10 min. The 1D SAXS profiles were obtained by circularly averaging the 2D data. Images were plotted as intensities (I) vs. q, where $q = (4\pi/\lambda)\sin(\theta)$, λ is the wavelength of the incident X-ray beam, and 2θ is the scattering angle.

Modeling Method. The nanocomposite morphology was simulated using the self-consistent field theory-density functional theory (SCFT-DFT) approach, first proposed by Thompson, Ginzburg, Matsen, and Balazs[5, 24] and subsequently modified by Ginzburg[25, 26] to explicitly include grafted ligands. The grafts are free to move on the particle surface, but cannot desorb from it. Within SCFT-DFT, the free energy of the binary mixture of BCPs and NPs can be written as,

$$\frac{FNv}{k_B TV} = -n_{HNP}\left(\frac{Q_{HNP}}{\phi_{HNP}V}\right) - n_{AB}\ln\left(\frac{Q_{AB}}{\phi_{AB}V}\right) + \frac{1}{V}\int dr \text{¿¿} \quad (1)$$

Here, v is the monomer reference volume, V is the total volume of the system, N is the degree of polymerization of the matrix diblock AB, $(\chi N)_{ij} = N\chi_{ij}$ for all species i and j; φ_i (**r**) is the local volume fraction of species I, and $\phi_i$is the average volume fraction (i = A, B, L, or P, where A and B are the two blocks of the diblock copolymer, L is ligand, and P is the particle core). The particle center density, ρ_P (**r**), is related to the local particle volume fraction φ_P (**r**) via the following expression,

$$\phi_P(r) = \frac{1}{Nv}\int dr'\,\rho_P(r')\Theta\left(R_P - |r - r'|\right) \quad (2)$$

Here, R_P is the particle radius, and Θ(x) is the Heaviside step function, $\Theta(x) = 0$, if $x < 0$, $\Theta(0) = 0.5$, and $\Theta(x) = 1$, if $x > 0$. For more detailed description of individual free energy terms and the approach to solving the self-consistency equations, see Refs. [5, 24-26]

RESULTS AND DISCUSSION

The chemical structure of the designed PS-*b*-P(MA-*r*-LA-*r*-OEGA) BCP consists of a PS coil block and an RCP comb block (Figure 1a). The BCP is designed as an analogue to the previously reported coil-comb supramolecule[27, 28] composed of polystyrene-*block*-poly(4-vinylpyridine) (PS-*b*-P4VP) and hydrogen-bonded small molecules 3-pentadecylphenol (PDP). The RCP block contains statistically randomly distributed monomers of MA and LA with an approximate molar ratio of 1:1. Since the supramolecule contains vinyl pyridine and PDP, both of which have polar groups (the nitrogen in the heterocycle and the hydroxyl group respectively), we selected to include a small amount of OEGA to add extra polar character to the RCP block, providing chemical heterogeneity. By incorporating LA into the polymer, alkyl-passivated NPs can be embedded within the RCP domain (Figure 1b) due to the favorable enthalpic interaction between their respective alkyl chains. The effect of the long alkyl tail of LA in the BCP resembles the long alkyl tail of PDP small molecules in the supramolecular system for NP assembly.[11] The alkyl tail of LA can also extend the backbone of the RCP block to a comb conformation.[29] A brush-like conformation may lower the polymer entanglement.[30, 31] MA was added to modulate the density of the long alkyl side chain in the RCP block. Low density limits the enthalpic interaction to incorporate NPs, while high density generates steric repulsion for the particle ligands to interact with the long alkyl side chains and also causes large polymer conformational entropy loss after NP addition. Hence, we chose a moderate value for the long alkyl side chain density by using an approximate 1:1 molar ratio of MA:LA monomers.

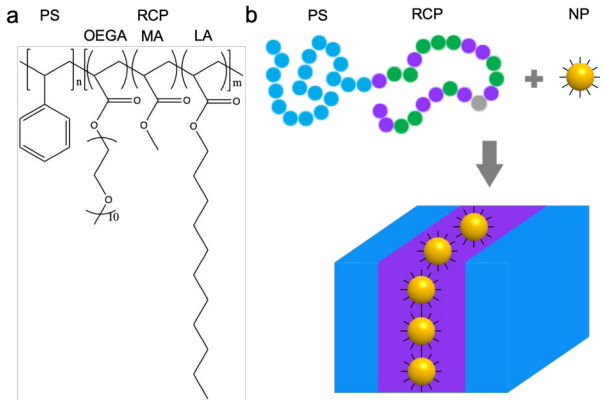

Figure 1. (a) Chemical structure of the PS-*b*-P(MA-*r*-LA-*r*-OEGA) polymer. (b) Schematic of the assembly of alkyl ligand-passivated NPs in the BCP nanocomposites (PS: blue; RCP: purple; NP: yellow).

Due to the similar reactivities of the styrene and acrylic monomers, we were able to pursue the synthesis of the BCPs using either monomer family as the first block. Our initial attempts started with the RCP block, composed of MA, LA, and a small amount of OEGA. These polymerizations were successful, producing a viscous gel. ^{1}H NMR analysis showed a polymer composition that was in good agreement with the initial monomer composition, and GPC showed a narrow molecular weight distribution, typical of RAFT polymerizations. These polymers were then extended with PS, yielding a powdery material containing both the RCP acrylates and PS as confirmed via NMR. GPC analysis enabled the evaluation of relative molecular weights and success of polymer extension to form the BCPs. The RCP blocks that have not been extended with styrene show only an RI peak, with no absorbance at 254 nm as expected. After extension, the RI peak shifts to an earlier elution, indicating an increase in hydrodynamic volume which correlates with larger molecular weight, as well as the appearance of a peak in the 254 nm absorbance at the same elution time, indicative of the presence of styrene. All samples show minimal to no absorbance in the 254 nm region outside of the primary

elution peak, suggesting minimal styrene homopolymer content present. However, the extension from the RCP did exhibit some undesirable features that led to us switching the sequence order in subsequent batches. Accurate weighing of required quantities of the RCP was practically difficult at this scale due to the gel like physical state and high viscosity. More importantly however, was the slow, and often inconsistent, growth of PS from the RCP block. By reversing the synthetic order, we were able to avoid working with gel in either step. Further, we did not experience any difficulty extending the PS blocks with RCP. This could also be due to the change in RAFT agent from a cyanomethyl dodecyl trithiocarbonate (RCP first) to 2-(Dodecylthiocarbonothioylthio)-2-methylpropionic acid (PS first). However, this seems unlikely given the fact that the two RAFT agents are structurally equivalent once the R group has fragmented off, a step that must happen early in the synthesis of the first block to provide RAFT control. A more likely cause is differences in the stability of the RCP-RAFT compound toward fragmentation compared with the PS-RAFT compound. Further investigation of these questions was considered beyond the scope of this work. Detailed NMR and GPC analysis of the polymers can be found in the Supplemental Information.

The characteristics of the synthesized PS-*b*-P(MA-*r*-LA-*r*-OEGA) BCPs are listed in Table 1. BCPs are coded according to the increasing f_{RCP} and the total molecular weight (M_n). M_n of the BCPs ranges from 40 kg/mol to 90 kg/mol, and f_{RCP} changes from 0.31 to 0.62. The polymer dispersity (Đ) ranges from 1.09 to 1.29 for the first synthesized blocks, and from 1.17 to 1.63 for the BCPs. The molar percentage of OEGA in the RCP domain is low and varies from 1% to 5%. The degree of polymerization (N) is calculated based on the M_n of the two blocks and the molar ratio of the monomers in the RCP block.

Table 1. PS-*b*-P(MA-*r*-LA-*r*-OEGA) Polymers Used in the Present Study

Polymer	PS/RCP (kg/mol)	**First** Block **Đ**	BCP **Đ**	f_{RCP}	RCP Composition Molar Ratio (MA:LA:OEGA)	N	Morphology
P1	57.2/26.5	1.27	1.57	0.31	50:49:1	707	L
P2	59.8/30.1	1.14	1.62	0.32	50:47.5:2.5	759	L
P3	58.3/31.9	1.17	1.63	0.32	50:45:5	817	L
P4	32.2/43.6	1.18	1.17	0.57	50:49:1	574	C+L
P5	22.7/30.8	1.29	1.57	0.60	50:47.5:2.5	407	M
P6	15.8/25.7	1.09	1.30	0.61	50:49:1	312	C
P7	15.7/25.7	1.09	1.20	0.62	50:49:1	310	C

Note: L: lamellae; C: cylinders; M: mixed morphologies, train-track.

The RCP block is the first synthesized block in P1, P2, P3, P5, P6 and P7; the PS block is the first synthesized block in P4.

The phase behavior of the bulk PS-*b*-P(MA-*r*-LA-*r*-OEGA) polymers listed in Table 1 was investigated after thermal annealing at 150 ºC for 48 hr. BCPs show disordered or short-range ordered structures directly after slow solvent evaporation as indicated by the indistinct or broad peaks in the SAXS profiles (Figure S1a). The differential scanning calorimetry (DSC) heating curve of P2 (Figure S1b) shows a melting temperature of the RCP block at -13 ˚C and a glass transition temperature of the PS block at ~100-110 ˚C. Long-range ordered morphologies were observed in the BCPs after thermal annealing as shown in the TEM images (Figure 2a-2g). The PS domain was stained by RuO_4 vapor as the dark regions.[32] P1, P2 and P3 exhibit lamellar morphologies; P4 and P5 show mixed cylindrical/lamellar morphologies; P6 and P7 display cylindrical morphologies. The average macroscopic morphologies and periodicities of the representative BCPs were analyzed based on the SAXS profiles (Figure 2i). P1, P2 and P3 have similar M_n ~90 kg/mol and f_{RCP} ~0.32. All the three polymers show lamellar morphologies and periodicities larger than 58 nm. P6 and P7 have M_n ~40 kg/mol and f_{RCP} ~0.62. Both polymers exhibit hexagonally packed PS cylindrical morphologies and the similar periodicity of 28 nm.

Complex structures were observed in P4 and P5 with f_{RCP} ranging from 0.57 to 0.6. P4 with M_n ~75 kg/mol shows mixed PS cylindrical and lamellar morphologies with periodicities of 34 nm and 36 nm, respectively. Based on the analysis of the TEM images and the SAXS profile, cylinder is the majority structure and lamella is the minority structure. More details about the mixed morphologies of P4 are shown in Figure S2. P5 with M_n ~53 kg/mol and f_{RCP} ~0.6 exhibits "train-track" morphology and a periodicity of 37 nm. The train-track morphology mainly contains lamellar structures with certain regions rich in short-range ordered cylindrical structures or line-bridging defects[33] (Figure 2h), essentially mixed morphologies of lamellar and cylindrical structures. The SAXS profile of P5 has a small first order peak and no well-defined high order peaks, which possibly reflects the mixed morphologies[34] and the relatively large Đ in P5. The absence of several high order peaks in P4 could also be attributed to the mixed morphologies. The small first order peaks in P1 probably result from the rough interfaces due to larger Đ in the P1-P3 polymers.

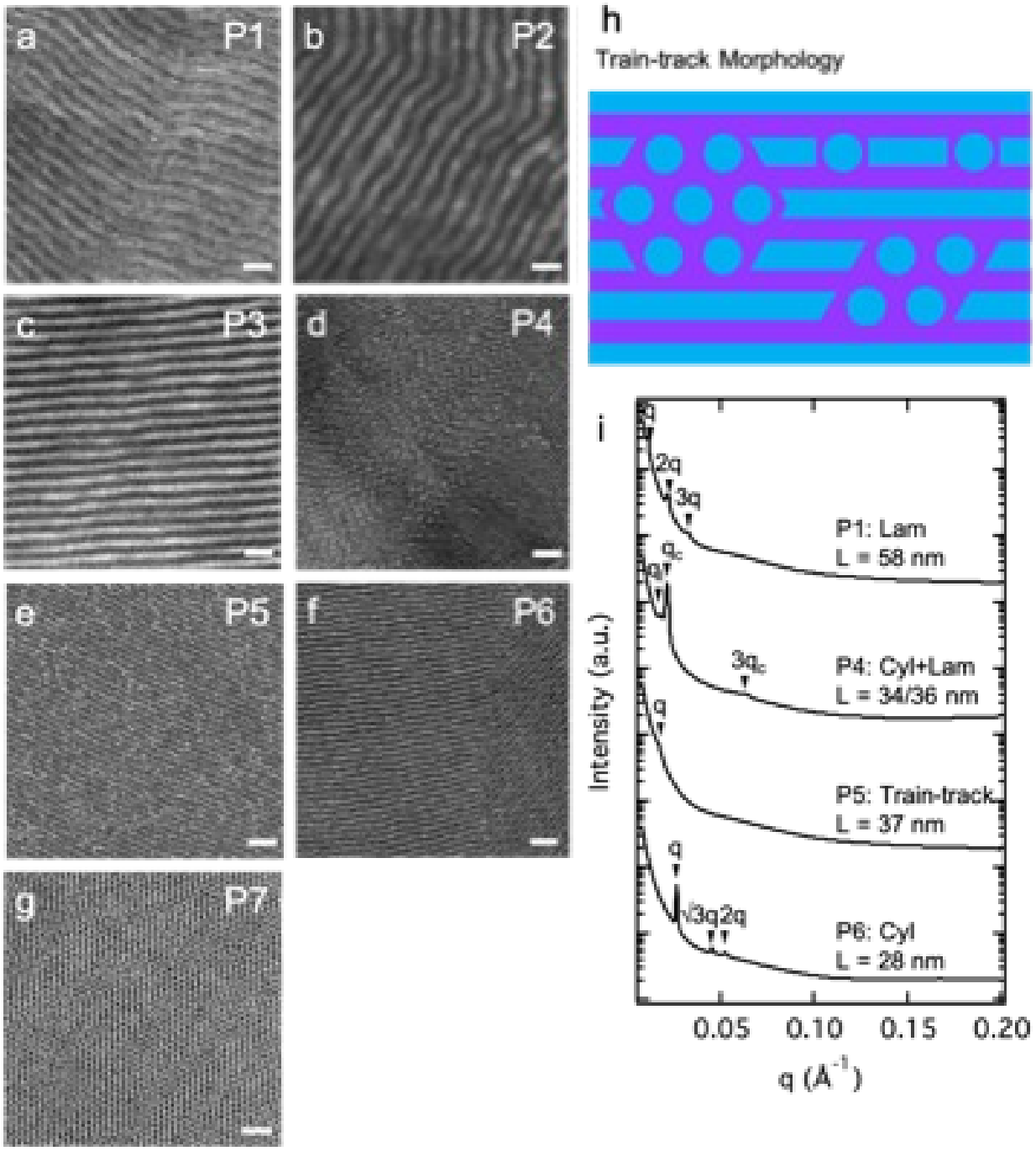

Figure 2. TEM images of PS-*b*-P(MA-*r*-LA-*r*-OEGA) bulk samples after thermal annealing at 150 ºC for 48 hr. The BCP morphologies in (a-c) are lamellae, (d-e) are mixed PS cylinders/lamellae, and (f-g) are PS cylinders. The PS domain is stained by RuO_4 as the dark regions (scale bar: 100 nm). (h) Schematic of the "train-track" morphology in P5 (PS: blue; RCP:

purple). (i) The corresponding SAXS profiles of the representative polymers with different morphologies.

We elected to remove the OEGA from the RCP block in the subsequently synthesized PS-*b*-P(MA-*r*-LA) BCPs as listed in Table 2. The phase behavior of the three BCPs was also studied after thermal annealing at 150 ºC for 48 hr. Figure 3 shows the TEM images and SAXS profiles of P8, P9 and P10 polymers. P8 with M_n ~35 kg/mol and f_{RCP} ~0.51 exhibits lamellar morphology with a periodicity ~25 nm. P9 with M_n ~43 kg/mol and f_{RCP} ~0.59 forms train-track morphology with a periodicity ~31 nm. The SAXS profile of P9 shows a small first order peak similar to P5, and broad high order peaks due to the mixed morphologies in the BCP. The Đ of P9 is not the largest among P8-P10 polymers and is smaller than P5. Thus, the formation of the train-track morphology cannot be solely attributed to the polydispersity of the polymers. P10 with M_n ~60 kg/mol and f_{RCP} ~0.62 generates cylindrical morphology with a periodicity ~41 nm. In the current scope of the work, there is no significant impact from the varying OEGA fractions in the RCP block on the morphology of the BCPs. P1 (1% OEGA), P2 (2.5% OEGA) and P3 (5% OEGA) show lamellar morphologies and similar periodicities. P7 with no OEGA also shows long-range ordered lamellar morphology. Train-track morphology was observed in both P5 (2.5% OEGA) and P9 (no OEGA). Cylindrical morphology was observed in P6 (1% OEGA), P7 (1% OEGA) and P10 (no OEGA).

Table 2. PS-*b*-P(MA-*r*-LA) Polymers Used in the Present Study

Polymer	PS/RCP (kg/mol)	First Block Đ	Total Đ	f_{RCP}	RCP Composition Molar Ratio (MA:LA)	N	Morphology
P8	17.3/18.2	1.17	1.33	0.51	50:50	277	L
P9	18.3/25.2	1.14	1.34	0.59	50:50	331	M
P10	23.4/35.6	1.14	1.48	0.62	50:50	443	C

Note: L: lamellae; C: cylinders; M: mixed morphologies, train-track.

The PS block is the first synthesized block in all the three polymers.

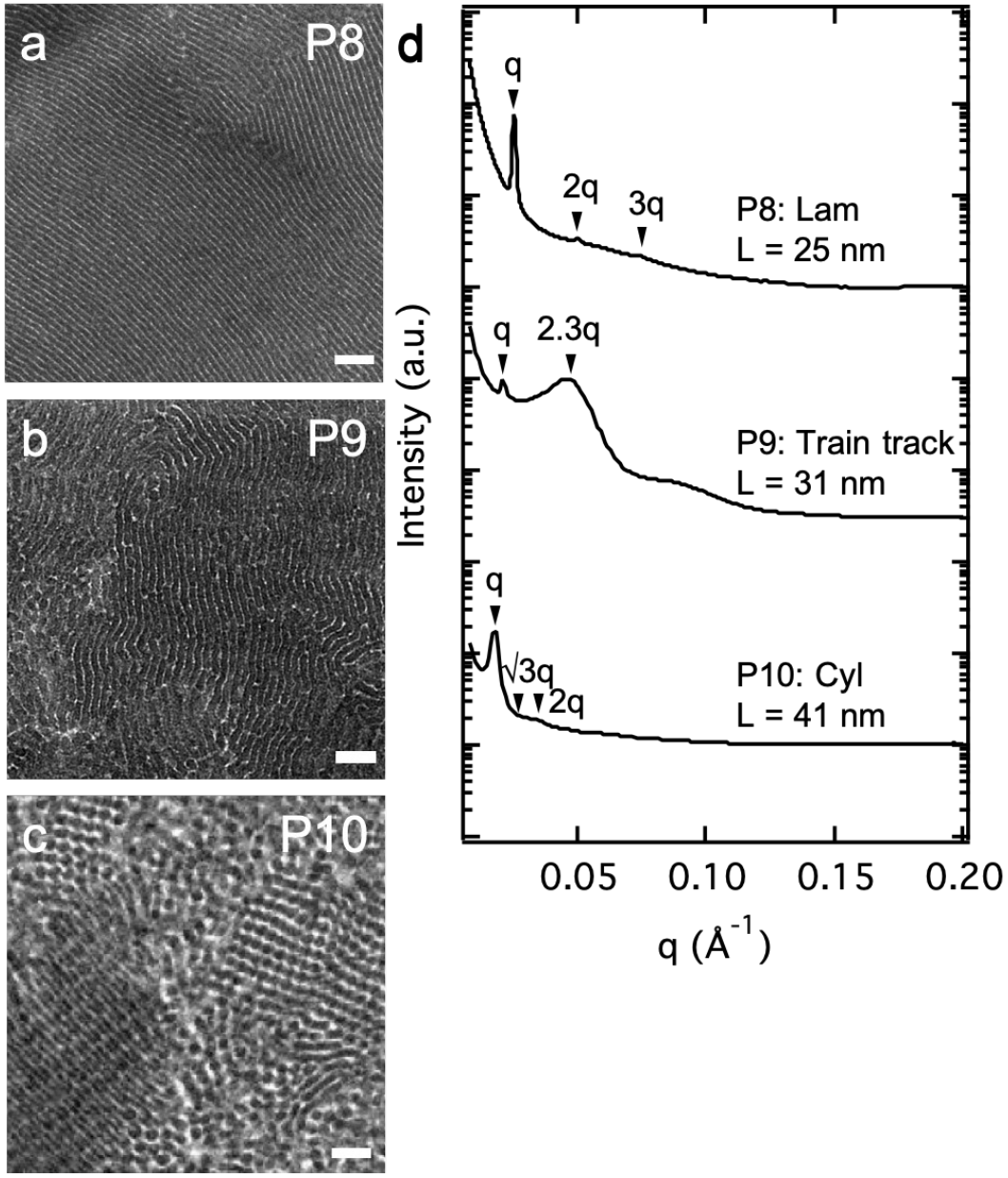

Figure 3. (a-c) TEM images of PS-*b*-P(MA-*r*-LA) bulk samples after thermal annealing at 150 ºC for 48 hr. The PS domain is stained by RuO_4 as the dark regions (scale bar: 100 nm). (d) The corresponding SAXS profiles of the three BCPs.

The morphology diagram of the ten PS-*b*-P(MA-*r*-LA-*r*-OEGA) and PS-*b*-P(MA-*r*-LA) polymers (Figure 2 and 3) is summarized in Figure 4 as a function of f_{RCP} and N. Since the value

of the Flory-Huggins interaction parameter (χ) between the two blocks has uncertainty and is temperature-dependent, we use N instead of χN in the morphology diagram. For BCPs in the current study with f_{RCP} from 0.31 to 0.62, the morphology diagram can be categorized into three regimes: lamellae at low f_{RCP}, PS cylinders at high f_{RCP} and mixed structures in a narrow range of medium f_{RCP}. The phase diagram of linear symmetric coil-coil diblock copolymers were predicted to be symmetric and centered at $f = 0.5$.[35] The morphology diagram of these coil-comb BCPs shows strong asymmetry with enhanced stability of PS cylinders or mixed structures at relatively low f_{RCP} compared to linear BCPs. Theoretically, asymmetric chain conformations of the two blocks can result in asymmetry of the BCP phase diagrams and may stabilize metastable states.[36] Highly asymmetric phase diagram was experimentally observed in poly(1,2-octylene oxide)-*block*-poly(ethylene oxide) (POO-*b*-PEO), a similar coil-brush BCP with strong conformational asymmetry.[29] In that system, lamellar phase was observed at $f_{POO} < 0.5$, and structures with curvatures were more widely observed when POO (with eight carbon alkyl tails) was the majority block. In the previously reported coil-comb PS-*b*-P4VP(PDP) supramolecular system, lamellar morphology was observed at $0.3 < f_{comb} < 0.53$,[28] and the comb block prefers to be on the convex side of a curved structure[37]. Similar to the above two systems, the morphology diagram in Figure 4 shows lamellar structures at f_{RCP} from 0.31 to 0.51, and structures with larger interfacial curvatures i.e. cylindrical and mixed structures, are more stabilized when the brush RCP is the majority block and on the convex side of a curved structure. Asymmetric phase diagrams are also commonly observed in bottlebrush BCPs[9, 38], where the asymmetry is not introduced by the different volume fractions of the two blocks, but rather, is driven by the asymmetry of the grafted side chain lengths[39]. This study further demonstrated that polymer chain architecture and conformation play important roles in the phase behavior of BCPs.

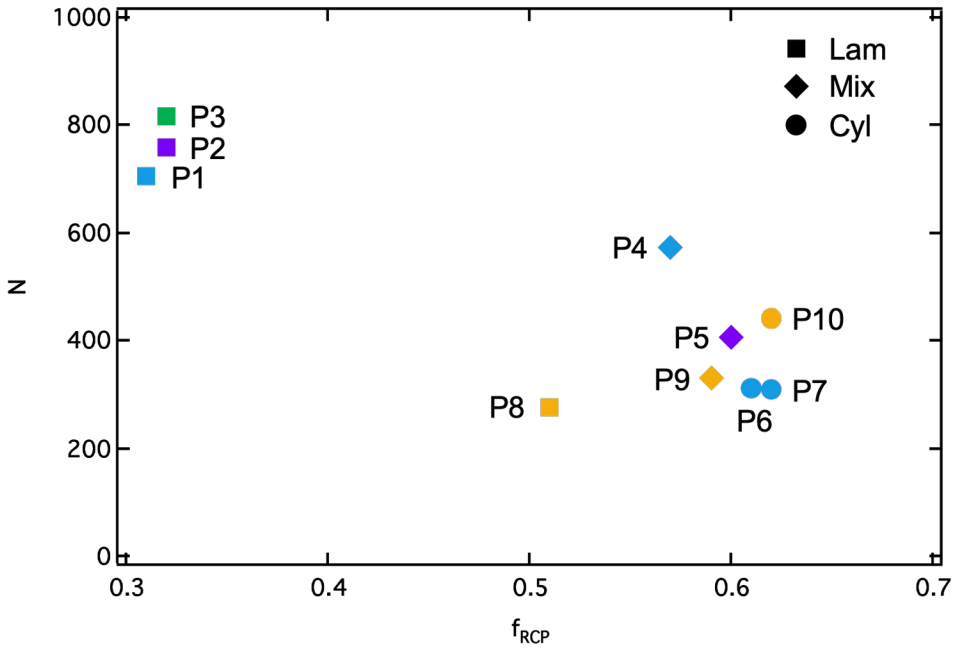

Figure 4. Morphology diagram of PS-*b*-P(MA-*r*-LA-*r*-OEGA) and PS-*b*-P(MA-*r*-LA) polymers after thermal annealing at 150 ºC for 48 hr as a function of RCP volume fraction (f_{RCP}) and degree of polymerization (N). Based on the varying molar percentage of OEGA in the RCP block, the polymers are marked as yellow (0%), blue (1%), purple (2.5%) or green (5%).

NP assembly in PS-*b*-P(MA-*r*-LA) polymers was investigated by blending P8, P9 and P10 polymers with alkyl ligand-passivated 5 nm ZrO_2 NPs. The NPs have an average core diameter of 5.2 nm and an average interparticle distance of 7.2 nm on TEM grids (Figure S3). These three polymers were selected because they represent the lamellar, mixed and cylindrical morphologies, respectively. Enthalpically, the favorable Van der Waals interactions between the alkyl ligands on NPs and the alkyl tails in LA should keep the NPs in the RCP domain. Entropically, the ratios between the NP diameter (d_{NP}) (including particle core and ligand shell) to the matrix periodicity (L) are 0.29, 0.23 and 0.18 for P8, P9 and P10 nanocomposites,

respectively. d_{NP}/L is one of the critical parameters that determine the entropic penalties associated with deforming the polymer chains after NP incorporation and the distribution of NPs within the domains.[1, 5, 13] In thin film nanocomposites, NPs with $d_{NP}/L > 0.3$ even segregated on film surfaces due to large entropic penalties.[13]

TEM images in Figure 5a-5c show the assembly of 2 vol% of NPs in P8, P9 and P10 nanocomposites after thermal annealing at 150 ºC for 48 hr. NPs are selectively incorporated in the RCP domain with good dispersion. NPs pack into hexagons surrounding the PS cylinders in P8 (Figure 5a) and P10 (Figure 5c) nanocomposites. In many regions, NPs cannot fully fill the RCP matrix due to the insufficient quantity. Based on SAXS analysis (Figure 5d), NPs assemble into cylindrical morphologies with a periodicity of 32 nm in P8 nanocomposite and a periodicity of 43 nm in P10 nanocomposite. Since the pristine P9 BCP forms mixed morphologies (Figure 3b), the packing order of NPs in P9 nanocomposite (Figure 5b) is low, and the NPs organize into complicated morphologies. The SAXS profile of P9 nanocomposite could reflect the averaged results from the mixed short-range ordered morphologies with an average periodicity of 34 nm. The addition of NPs expands the periodicities of P9 and P10 slightly from 31 nm to 34 nm and from 41 nm to 43 nm, but expands the periodicity of P8 obviously from 25 nm to 32 nm.

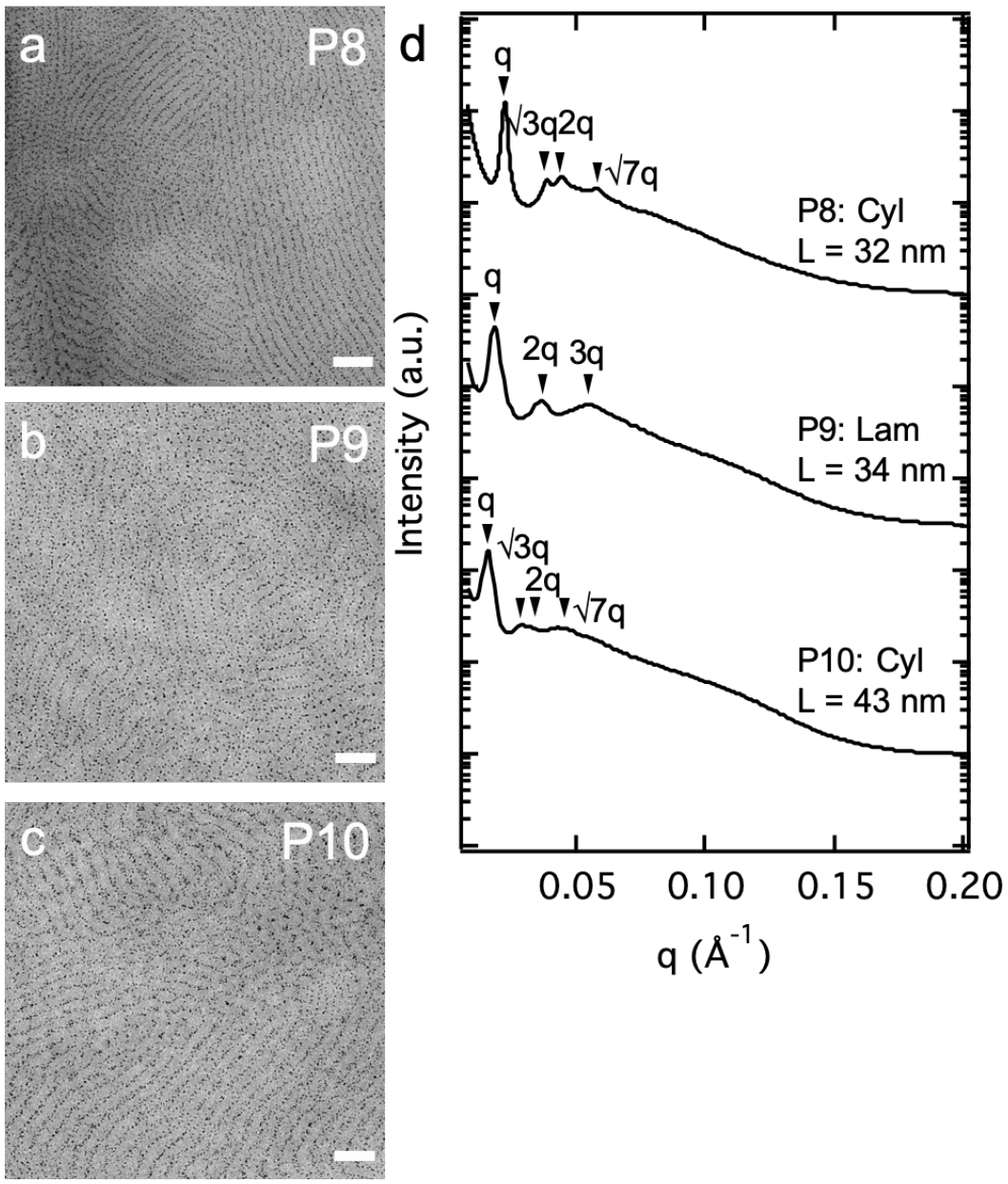

Figure 5. (a-c) TEM images of P8, P9 and P10 PS-*b*-P(MA-*r*-LA) nanocomposites containing 2 vol% of 5 nm ZrO_2 NPs after thermal annealing at 150 ºC for 48 hr (scale bar: 100 nm). (d) The corresponding SAXS profiles of the three nanocomposites.

After the addition of 2 vol% of NPs, P8 nanocomposite shows an order-to-order morphological transition from lamellae (Figure 3a) to PS cylinders (Figure 5a) with an obviously expanded periodicity from 25 nm to 32 nm. NP-induced order-to-order phase transition in BCP

nanocomposites has been widely reported.[8, 9, 40-42] The addition of NPs increases the volume fraction of the host domain and reduces polymer conformational entropy. The localization of NPs in the BCP can induce stress at the interfaces, increase the interfacial curvature between the two blocks, and thus shift the nanocomposite morphology from the lamellar regime toward the cylindrical regime.[6] P8 has the smallest periodicities and largest d_{NP}/L ratio among the three polymers. NP addition in the RCP domain introduces the largest polymer conformational entropic penalties among the three polymers. Although the addition of 2 vol% of NPs only slightly increases f_{RCP} from 0.51 to ~0.53, it still effectively increases the interfacial curvature and induces an order-to-order morphological transition in the nanocomposite. Besides ZrO_2 NPs, 2 vol% of 4 nm Au NPs coated by oleylamine were also successfully incorporated in the P2 and P4 PS-*b*-P(MA-*r*-LA-*r*-OEGA) nanocomposites as shown in Figure S4, where P2 and P4 contain 2.5% and 1% OEGA in the RCP domain, respectively. In summary, NPs coated by alkyl ligands with 8 or 18 carbons were effectively dispersed in the RCP block containing alkyl side chains with 12 carbons. The existence of a small amount of OEGA does not visually affect the compatibility of NPs with the RCP domain.

NP loading in P8 nanocomposite was varied from 1 vol% to 4 vol% to further investigate the phase behavior. TEM images in Figure 6a-6c show P8 nanocomposites after thermal annealing at 150 ºC for 48 hr. At 1 vol% particle loading (Figure 6a), NPs distribute homogeneously in the RCP lamellae, indicating large NP translational entropy in the nanocomposite. NPs form linear arrays in the center of the RCP domain with a periodicity 30 nm. The periodicity was measured as the largest distance between two neighboring NP arrays in the TEM images. However, it is hard to identify the nanocomposite morphology due to the low particle loading and the incomplete particle filling. The more apparent order-to-order

morphological transition occurs at 2 vol% particle loading, where the nanocomposite forms cylindrical structures with a periodicity of 32 nm (Figure 6b). The full width at half maximum (FWHM) values of NP distribution across the RCP domain are 6.4 nm and 7.5 nm at 1 vol% and 2 vol% particle loadings, respectively (Figure 6d-6e). NPs have narrow distribution in the host domain at 1 vol% particle loading, while NPs become less confined in the domain center when the particle loading is increased to 2 vol%. Figure 6f clearly shows the arrangement of NPs around the hexagonally packed PS cylinders forming hexagonal grids within the RCP domain. No long-range order was observed in the nanocomposite with 4 vol% of NPs (Figure 6c).

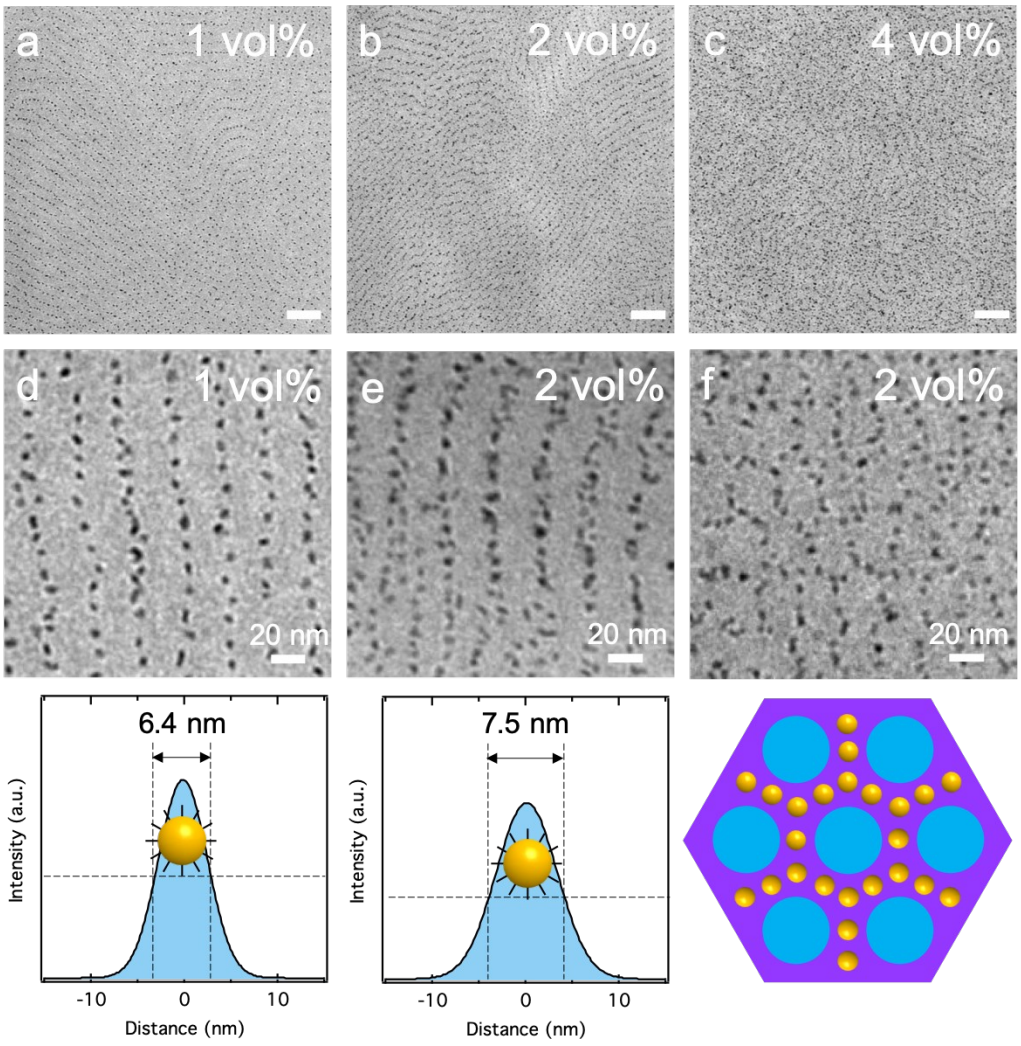

Figure 6. (a-c) TEM images of P8 PS-*b*-P(MA-*r*-LA) containing (a) 1 vol%, (b) 2 vol% and (c) 4 vol% of 5 nm ZrO_2 NPs after thermal annealing at 150 ºC for 48 hr (scale bar: 100 nm). (d-e) TEM analysis of NP distribution in the RCP domain of the nanocomposites containing (d) 1 vol % and (e) 2 vol% of NPs. (f) TEM image and schematic of the hexagonal arrangement of NPs in the cylindrical nanocomposite with 2 vol% of NPs (PS: blue; RCP: purple; NP: yellow).

In situ SAXS measurements of P8 polymer and nanocomposites were performed by varying the particle loading from 0 vol% to 4 vol% and the annealing temperature from 90 ˚C to 180 ˚C (Figure 7a-7d). The periodicities of the samples were converted from the q values of the first order peaks in the SAXS profiles (Figure 7e). The grain sizes of the samples were calculated using the Scherrer equation[43] based on the FWHM of the first order peaks (Figure 7f). All the samples at 25 ˚C before thermal annealing have broad first order peaks and do not show high order peaks, indicating poor order in the samples right after slow solvent evaporation. Based on DSC analysis, T_g of the polymer is ~95 ˚C (Figure S5). As the annealing temperature increases above 90 ˚C, both the periodicities and grain sizes of the samples start to evolve. The periodicities keep almost constant after 150 ˚C, and the grain sizes decrease slightly after 170 ˚C. 150 ˚C was chosen as the annealing temperatures for all the samples in the above static measurements, because both BCP and nanocomposite show relatively large grain sizes and stable periodicities at 150 ˚C in the temperature range of 90-180 ˚C during the *in situ* measurements. In fact, P8-P10 BCPs show states with low order or disorder after thermal annealing at 190 ˚C for 48 hr (Figure S6), indicating the BCPs are close to or above the order-disorder transition (ODT) temperature at 190 ˚C. In P8 BCP (Figure 7a), high order peaks start to appear ~110-120 ˚C, indicating a lamellar morphology of the polymer with a periodicity ~25 nm, consistent with

Figure 3a and 3d. At 1 vol% particle loading (Figure 7b), the nanocomposite forms cylindrical morphology with a periodicity of 30 nm based on the first order peak in the SAXS profile and the TEM image in Figure 6a. The incomplete particle filling may explain the absence of √3q peaks indicative of cylindrical structures, and only 2q peaks are present at 110-170°C. With 2 vol% particle loading (Figure 7c), sharp high order peaks are observed at ~150-180 °C, indicative of long-range ordering of the NPs with the nanocomposite forming a cylindrical morphology with a periodicity of 32 nm. The results agree well with Figure 5b, 5d and 6b. At 4 vol% particle loading, the grain size does not increase much after thermal annealing as indicated by the low order in the TEM image (Figure 6c). The broad high order peaks reveal poor order in the nanocomposite, probably owing to jammed states at high particle loading in this temperature range.

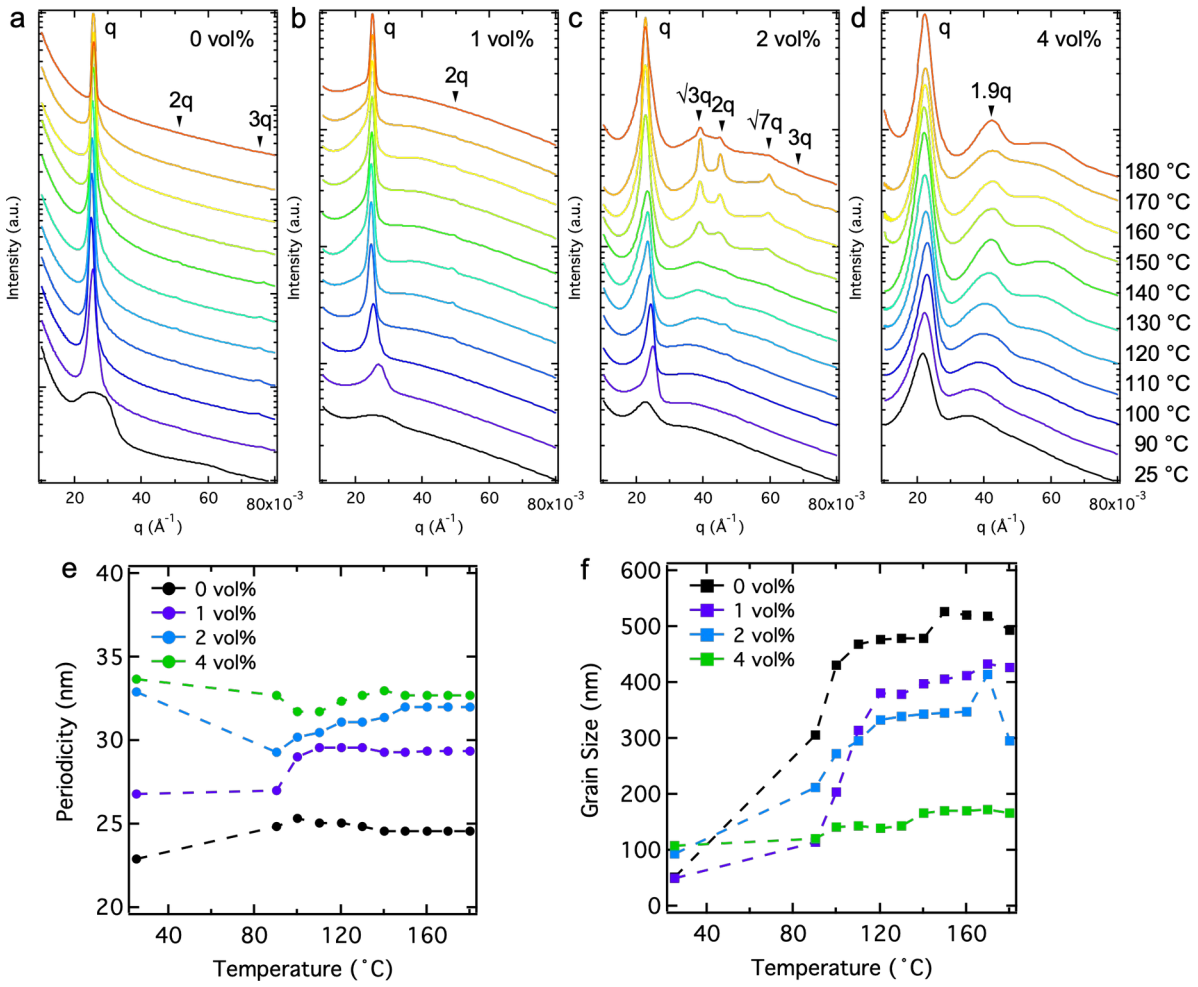

Figure 7. (a-d) *In situ* SAXS profiles of P8 PS-*b*-P(MA-*r*-LA) containing (a) 0 vol%, (b) 1 vol%, (c) 2 vol% and (d) 4 vol% of 5 nm ZrO_2 NPs. The change of (e) periodicity and (f) grain size as a function of annealing temperature in the P8 polymer and nanocomposites.

Both enthalpic and entropic factors need to be finely modulated to construct BCP nanocomposites containing hierarchically assembled NP arrays with high spatial resolution. To date, many efforts have been focused on the polymer or NP ligand modification to increase NP/polymer enthalpic interactions[44, 45]; or on tuning the polymer architecture[9, 11] or the ratio of NP size to polymer periodicity[1, 13] to adjust the entropic contributions. In the current study, we designed the coil-comb BCP with covalently bonded long alkyl side chains as an analogue to the

previously reported coil-comb PS-*b*-P4VP(PDP) supramolecule[27] with hydrogen bonded long alkyl side chains. 5 nm NPs coated by alkyl ligands were successfully included in the RCP domain forming ordered morphologies in the nanocomposites. Although the alkyl side chain density in the RCP domain is only ~50%, less than half of that in the supramolecule[11], the favorable Van der Waals enthalpic interactions between the alkyl ligands and side chains are still large enough to selectively incorporate the NPs in the RCP block. Entropically, the localization of NPs can be controlled by the ratio of d_{NP}/L[1] and the polymer chain architecture[4]. As d_{NP}/L is ~0.23 in the P8 nanocomposites (Figure 7a-7b), it is energetically favorable for the NPs to be located in the center of the host block to minimize the entropic penalties associated with deforming the polymer chains.[1]

We also simulated the morphologies of P8/ZrO_2 nanocomposites as a function of the NP volume fraction. While the simulation is not aimed at determining the exact phase behavior, it is used to provide a qualitative description of the observed morphologies and, in particular, the transition from the lamellar structure for the pure BCP to the cylindrical one for the nanocomposite. While a similar transition was found in earlier diblock/NP simulations,[46] the actual arrangement of NPs around the cylinders was never investigated in detail. In the following, we will describe how the particles arrange around the PS cylinders and what factors influence this arrangement.

The P8 BCP is represented as an AB-diblock, where A is the styrene block, and B is the acrylic block. The composition parameter f_A is set to 0.38, and the segregation strength $(\chi N)_{AB}$ = 35.6, so that the equilibrium morphology of the pure diblock is lamellar, but very close to the lamellar-hexagonal transition.[35] (The actual volume fraction of the styrene block is about 0.5 rather than 0.38. The effective value of f_A used in the simulation reflects the fact that the order-

disorder transition line is asymmetric in composition due to the fact that the acrylic block is not a simple linear chain, but a brush-like polymer). The reference volume v = 1 nm^3 and corresponds to the unit mass 250 g/mol. This parameterization results in the lamellar period D = 24 ± 1 nm, consistent with experimental data. We parameterize ZrO_2 NP as a "hairy nanoparticle" (HNP) with radius R_P = 2.55 nm, having n = 10 grafted ligands of length L = 15. The Flory-Huggins interaction parameters are given in Table 3.

Table 3. Flory-Huggins Interaction Parameters Used in the Simulation

Species	A	B	L	P
A	0	0.247	0.247	0.5
B	0.247	0	0	0.5
L	0.247	0	0	0.5
P	0.5	0.5	0.5	0

For each nanoparticle volume fraction (4, 8, 12, and 16% for the total HNP loading; 1.5, 3, 4.5, and 6% inorganic core volume fractions), we run simulations starting from five initial configurations as shown in Figure 8a. The first configuration has a square XY-cross-section, and a single HNP is placed at the center of the box. In the four remaining configurations, the XY-cross-section is rectangular, with n_x:n_y = 7:4 ≈ $\sqrt{3}$. The nanoparticles are placed in the central layer (z = n_z/2). The second configuration corresponds to 2 HNPs per unit cell, the third one to 4 HNPs per unit cell, the fourth one to 6 HNPs per unit cell, and the last one to 10 HNPs per unit cell. The initial densities of all polymer and ligand species outside the nanoparticle-containing cells are uniform. In all cases, the unit cell dimension in the Z-direction, n_z, is varied, while the box parameters in the X and Y directions are kept constant. The lowest free energy (as function of n_z) is calculated for each morphology, and a global minimum is then selected by comparing all those individual minima.

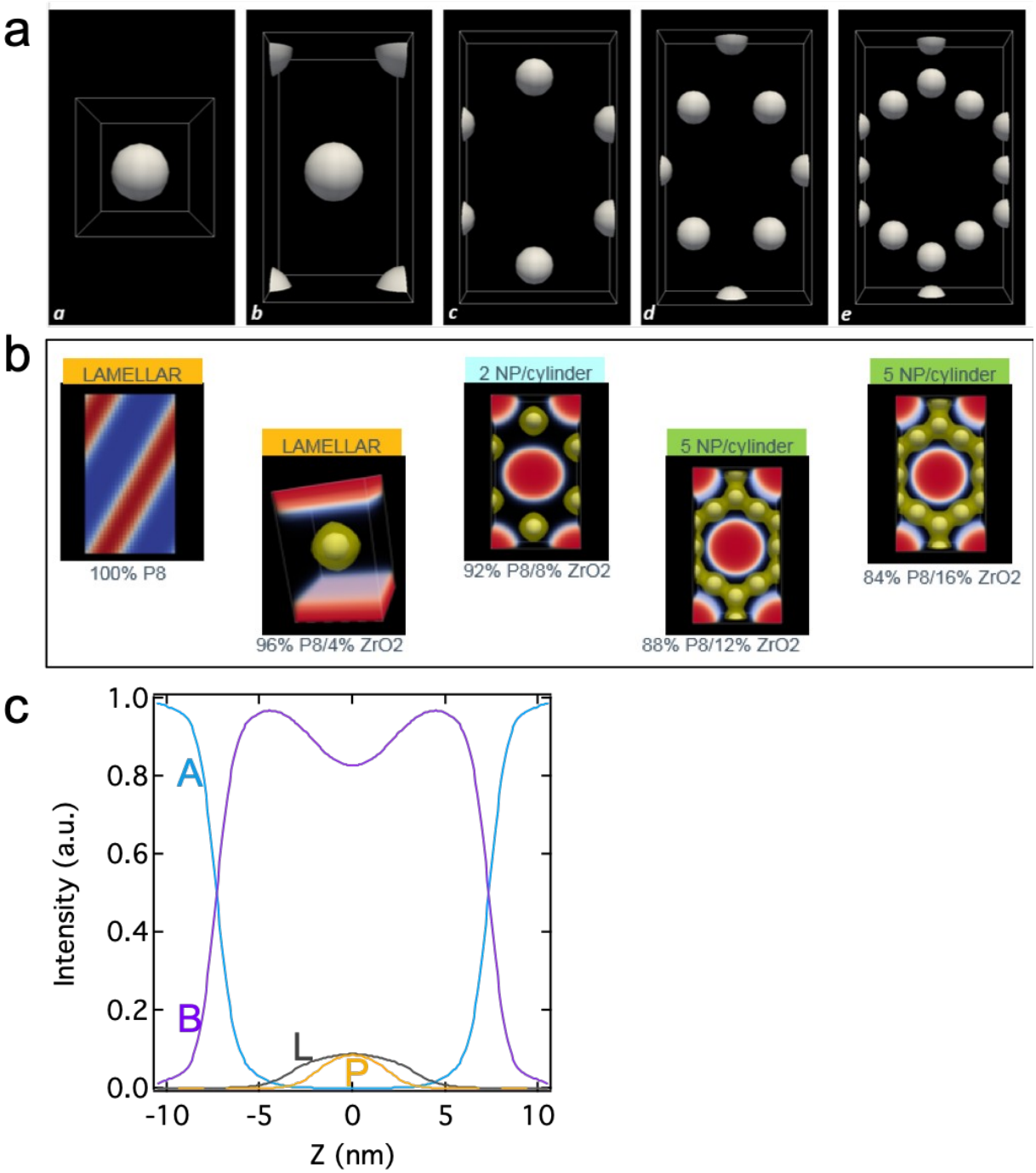

Figure 8. (a) Initial configurations with 1, 2, 4, 6 and 10 HNP per unit cell. In all cases, the view is in the +Z direction. The spheres correspond to φ_P = 0.5 level sets. (b) Morphologies of BCP/NP nanocomposites. The 100% P8 was calculated using 2D-SCFT, the rest were 3D simulations. Red corresponds to PS-rich domains, blue or black to acrylic domains. The light

green represents the ligands, and the white spheres correspond to the particles. The 4% ZrO_2 view is tilted, while the rest are viewed along Z-axis. (c) Density profiles of polymers, ligands, and particles for the 96% P8/4% ZrO2 nanocomposite with lamellar morphology.

The simulation results are shown in Figure 8b. Here, red corresponds to A-rich (polystyrene) domains, light green corresponds to ligand-rich regions, and the white spheres inside the ligand regions represent the particles density (level set surfaces corresponding to φ_P = 0.5). At low particle loadings of 0 and 4 vol%, the polymer maintains the lamellar morphology. As the particle concentration is increased, the effective volume fraction of the styrene block drops below the effective threshold for the lamellar-hexagonal transition, and the nanocomposite morphology changes to cylindrical. At first, each NP is "shared" between three adjacent PS cylinders, so that there are total of 2 NP per cylinder at 8 vol% particle loading; this arrangement has been recently discovered by Jenzcyk et al.[47] As the NP concentration is increased further, the morphology changes first to 3 NP per cylinder (seen only as metastable in our simulations but probably stable under some other conditions) and then to 5 NP per cylinder at 12 and 16 vol% particle loadings. The last arrangement is consistent with our experimental observations.

To better quantify the distribution of various components, in Figure 8c we plot the density profiles for the lamellar case (4% HNP). The particles are segregated into the center of the P(MA-*r*-LA) lamellar domain; the crowding at the center pushes the polymer block towards the edges, creating a "dip" or "crater". This type of material distribution was already found in the earlier SCFT-DFT simulations of "bald" nanoparticles in lamella-forming AB-diblocks;[5, 24] our current result is in excellent agreement with those studies. For the various hybrid cylindrical morphologies, plotting density profiles would require cross-sections in various directions (to

show the distributions between the centers of adjacent PS cylinders or along the major axes of the unit cell), and is beyond the scope of this initial study.

In summary, we demonstrated that for the P8/ZrO_2 nanocomposite, the observed transition between the lamellar and cylindrical morphologies upon increasing NP concentration can be successfully modeled using SCFT-DFT approach. The transition is driven by the strong preference of the particles towards the P(MA-*r*-LA) block; the effective volume fraction of the PS block is thus reduced and eventually (at HNP volume fraction 5-7% in the simulation and about 1.25-1.75% in experiment) drops below the effective lamellar-hexagonal boundary. The idealized structure corresponding to a monolayer with 5 particles per PS cylinder has been shown to be the equilibrium morphology, at least at sufficiently high nanoparticle volume fractions (12% and above). The SCFT-DFT simulations described here were designed primarily to explore the qualitative mechanisms of self-assembly in the diblock/hairy nanoparticle mixtures, not to compute the phase diagram with a quantitative precision. The initial results shown here elucidated the morphology and phase behavior for a given BCP (P8) and NP (modified ZrO_2). Further calibration of the model for the current system and its extension to other polymers in this study will be a subject of future work.

CONCLUSIONS

In summary, we designed a BCP containing a coil PS block and a comb RCP block with acrylate monomers for the assembly of NPs. BCPs of different molecular weights and RCP volume fractions were synthesized using RAFT polymerization. Lamellar, PS cylindrical, and mixed morphologies were observed in those BCPs after thermal annealing. The morphology diagram of the coil-comb BCP show strong asymmetry, where lamellar morphologies were

observed at f_{RCP} = 0.31-0.51, and morphologies with curvatures were more widely observed when RCP is the majority block and on the convex side of the structures. Those observations are similar to the results from microphase separated systems with asymmetric chain conformations between the two polymer blocks, like other coil-brush BCPs, coil-comb supramolecules and bottlebrush BCPs. 4-5 nm alkyl ligand-passivated NPs were successfully incorporated in the RCP domain with alkyl tails through preferential enthalpic interactions. An order-to-order morphological transition was observed after the addition of only 1-2 vol% of NPs in the BCP with the smallest periodicity, due to the change of polymer conformational entropy and the interfacial curvature after NP incorporation. NPs are confined in the center of the RCP block with relatively narrow spatial distribution to reduce the entropic penalties associated with deforming the comb RCP block. SCFT-DFT simulations qualitatively described the observed morphologies and phase transitions in the nanocomposites. These studies provide fundamental understandings about the effects of polymer chain architecture on the phase behavior of BCPs and nanocomposites, and give guidance to design new BCPs for the fabrication of functional nanocomposite materials.

ACKNOWLEDGEMENTS

This work was funded by DOW Chemical and the U.S. Department of Energy, Office of Science, Office of Basic Energy Sciences, Materials Sciences and Engineering Division, under Contract DE-AC02-05-CH11231 (Organic-Inorganic Nanocomposites KC3104) SAXS studies at Advanced Photon Source was supported by the US Department of Energy, Office of Science, Office of Basic Energy Sciences, under Contract DE-AC02-06CH1135. SAXS studies at the Advanced Light Source is supported by the U.S. Department of Energy, Office of Science, Office of Basic Energy Sciences, of the U.S. Department of Energy under Contract DE-AC02-05CH11231.

CONFLICT OF INTEREST STATEMENT

We have filed a patent prevision on the composite systems in conjunction with DOW Chemical.

SUPPORTING INFORMATION

Supplemental SAX profiles, TEM images, TGA analysis, ^{1}H-NMR spectra, and GPC chromatograms of synthesized polymers. This material is available free of charge via the Internet at http://pubs.acs.org.

REFERENCES

1. Bockstaller, M. R.; Lapetnikov, Y.; Margel, S.; Thomas, E. L., Size-Selective Organization of Enthalpic Compatibilized Nanocrystals in Ternary Block Copolymer/Particle Mixtures. *J. Am. Chem. Soc.* **2003,** *125* (18), 5276-5277.
2. Kim, B. J.; Bang, J.; Hawker, C. J.; Chiu, J. J.; Pine, D. J.; Jang, S. G.; Yang, S. M.; Kramer, E. J., Creating surfactant nanoparticles for block copolymer composites through surface chemistry. *Langmuir* **2007,** *23* (25), 12693-12703.
3. Jang, S. G.; Khan, A.; Hawker, C. J.; Kramer, E. J., Morphology Evolution of PS-b-P2VP Diblock Copolymers via Supramolecular Assembly of Hydroxylated Gold Nanoparticles. *Macromolecules* **2012,** *45* (3), 1553-1561.
4. Gai, Y.; Lin, Y.; Song, D. P.; Yavitt, B. M.; Watkins, J. J., Strong Ligand-Block Copolymer Interactions for Incorporation of Relatively Large Nanoparticles in Ordered Composites. *Macromolecules* **2016,** *49* (9), 3352-3360.
5. Thompson, R. B.; Ginzburg, V. V.; Matsen, M. W.; Balazs, A. C., Predicting the mesophases of copolymer-nanoparticle composites. *Science* **2001,** *292* (5526), 2469-2472.
6. Sarkar, B.; Alexandridis, P., Block copolymer–nanoparticle composites: Structure, functional properties, and processing. *Progress in Polymer Science* **2015,** *40*, 33-62.
7. Listak, J.; Hakem, I. F.; Ryu, H. J.; Rangou, S.; Politakos, N.; Misichronis, K.; Avgeropoulos, A.; Bockstaller, M. R., Effect of Chain Architecture on the Compatibility of Block Copolymer/Nanoparticle Blends. *Macromolecules* **2009,** *42* (15), 5766-5773.
8. Kim, B. J.; Chiu, J. J.; Yi, G. R.; Pine, D. J.; Kramer, E. J., Nanoparticle-induced phase transitions in diblock-copolymer films. *Adv. Mater.* **2005,** *17* (21), 2618-2622.
9. Song, D. P.; Lin, Y.; Gai, Y.; Colella, N. S.; Li, C.; Liu, X. H.; Gido, S.; Watkins, J. J., Controlled Supramolecular Self-Assembly of-Large Nanoparticles in Amphiphilic Brush Block Copolymers. *J. Am. Chem. Soc.* **2015,** *137* (11), 3771-3774.
10. Song, D.-P.; Li, C.; Li, W.; Watkins, J. J., Block Copolymer Nanocomposites with High Refractive Index Contrast for One-Step Photonics. *Acs Nano* **2016,** *10* (1), 1216-1223.
11. Zhao, Y.; Thorkelsson, K.; Mastroianni, A. J.; Schilling, T.; Luther, J. M.; Rancatore, B. J.; Matsunaga, K.; Jinnai, H.; Wu, Y.; Poulsen, D.; Fréchet, J. M. J.; Paul Alivisatos, A.; Xu, T., Small-molecule-directed nanoparticle assembly towards stimuli-responsive nanocomposites. *Nature Materials* **2009,** *8* (12), 979-985.
12. Kao, J.; Bai, P.; Chuang, V. P.; Jiang, Z.; Ercius, P.; Xu, T., Nanoparticle Assemblies in Thin Films of Supramolecular Nanocomposites. *Nano Lett.* **2012,** *12* (5), 2610-2618.

13. Kao, J.; Bai, P.; Lucas, J. M.; Alivisatos, A. P.; Xu, T., Size-Dependent Assemblies of Nanoparticle Mixtures in Thin Films. *J. Am. Chem. Soc.* **2013,** *135* (5), 1680-1683.
14. Kao, J.; Thorkelsson, K.; Bai, P.; Zhang, Z.; Sun, C.; Xu, T., Rapid fabrication of hierarchically structured supramolecular nanocomposite thin films in one minute. *Nat Commun* **2014,** *5*, 4053.
15. Fredrickson, G. H., Surfactant-Induced Lyotropic Behavior of Flexible Polymer-Solutions. *Macromolecules* **1993,** *26* (11), 2825-2831.
16. Dalsin, S. J.; Hillmyer, M. A.; Bates, F. S., Linear Rheology of Polyolefin-Based Bottlebrush Polymers. *Macromolecules* **2015,** *48* (13), 4680-4691.
17. J. Trazkovich, A.; F. Wendt, M.; M. Hall, L., Effect of copolymer sequence on structure and relaxation times near a nanoparticle surface. *Soft Matter* **2018,** *14* (28), 5913-5921.
18. Trazkovich, A. J.; Wendt, M. F.; Hall, L. M., Effect of Copolymer Sequence on Local Viscoelastic Properties near a Nanoparticle. *Macromolecules* **2019,** *52* (2), 513-527.
19. Hall, L. M.; Schweizer, K. S., Impact of Monomer Sequence, Composition and Chemical Heterogeneity on Copolymer-Mediated Effective Interactions between Nanoparticles in Melts. *Macromolecules* **2011,** *44* (8), 3149-3160.
20. Banerjee, D.; Schweizer, K. S., Controlling effective interactions and spatial dispersion of nanoparticles in multiblock copolymer melts. *Journal of Polymer Science Part B: Polymer Physics* **2015,** *53* (16), 1098-1111.
21. Beckingham, B. S.; Register, R. A., Synthesis and Phase Behavior of Block-Random Copolymers of Styrene and Hydrogenated Isoprene. *Macromolecules* **2011,** *44* (11), 4313-4319.
22. Peng, S.; Lee, Y. M.; Wang, C.; Yin, H. F.; Dai, S.; Sun, S. H., A Facile Synthesis of Monodisperse Au Nanoparticles and Their Catalysis of CO Oxidation. *Nano Res* **2008,** *1* (3), 229-234.
23. Beers, K. L.; Matyjaszewski, K., The atom transfer radical polymerization of lauryl acrylate. *J Macromol Sci Pure* **2001,** *38* (7), 731-739.
24. Thompson, R. B.; Ginzburg, V. V.; Matsen, M. W.; Balazs, A. C., Block copolymer-directed assembly of nanoparticles: Forming mesoscopically ordered hybrid materials. *Macromolecules* **2002,** *35* (3), 1060-1071.
25. Ginzburg, V. V., Polymer-Grafted Nanoparticles in Polymer Melts: Modeling Using the Combined SCFT–DFT Approach. *Macromolecules* **2013,** *46* (24), 9798-9805.
26. Ginzburg, V. V., Modeling the Morphology and Phase Behavior of One-Component Polymer-Grafted Nanoparticle Systems. *Macromolecules* **2017,** *50* (23), 9445-9455.
27. Ruokolainen, J.; Brinke, G. t.; Ikkala, O., Supramolecular Polymeric Materials with Hierarchical Structure-Within-Structure Morphologies. *Adv. Mater.* **1999,** *11* (9), 777-780.
28. Ruokolainen, J.; Saariaho, M.; Ikkala, O.; ten Brinke, G.; Thomas, E. L.; Torkkeli, M.; Serimaa, R., Supramolecular Routes to Hierarchical Structures: Comb-Coil Diblock Copolymers Organized with Two Length Scales. *Macromolecules* **1999,** *32* (4), 1152-1158.
29. Hamley, I. W.; O'Driscoll, B. M. D.; Lotze, G.; Moulton, C.; Allgaier, J.; Frielinghaus, H., Highly Asymmetric Phase Diagram of a Poly(1,2-octylene oxide)-Poly(ethylene oxide) Diblock Copolymer System Comprising a Brush-Like Poly(1,2-octylene oxide) Block. *Macromol Rapid Comm* **2009,** *30* (24), 2141-2146.
30. Paturej, J.; Sheiko, S. S.; Panyukov, S.; Rubinstein, M., Molecular structure of bottlebrush polymers in melts. *Sci Adv* **2016,** *2* (11).

31. Namba, S.; Tsukahara, Y.; Kaeriyama, K.; Okamoto, K.; Takahashi, M., Bulk properties of multibranched polystyrenes from polystyrene macromonomers: rheological behavior I. *Polymer* **2000,** *41* (14), 5165-5171.
32. Trent, J. S.; Scheinbeim, J. I.; Couchman, P. R., Ruthenium Tetraoxide Staining of Polymers for Electron-Microscopy. *Macromolecules* **1983,** *16* (4), 589-598.
33. Doerk, G. S.; Yager, K. G., Rapid Ordering in "Wet Brush" Block Copolymer/Homopolymer Ternary Blends. *Acs Nano* **2017,** *11* (12), 12326-12336.
34. Rancatore, B. J.; Kim, B.; Mauldin, C. E.; Frechet, J. M. J.; Xu, T., Organic Semiconductor-Containing Supramolecules: Effect of Small Molecule Crystallization and Molecular Packing. *Macromolecules* **2016,** *49* (3), 833-843.
35. Matsen, M. W.; Bates, F. S., Unifying weak- and strong-segregation block copolymer theories. *Macromolecules* **1996,** *29* (4), 1091-1098.
36. Matsen, M. W.; Bates, F. S., Conformationally asymmetric block copolymers. *J Polym Sci Pol Phys* **1997,** *35* (6), 945-952.
37. Vukovic, I.; ten Brinke, G.; Loos, K., Hexagonally Perforated Layer Morphology in PS-b-P4VP(PDP) Supramolecules. *Macromolecules* **2012,** *45* (23), 9409-9418.
38. Bolton, J.; Bailey, T. S.; Rzayev, J., Large Pore Size Nanoporous Materials from the Self-Assembly of Asymmetric Bottlebrush Block Copolymers. *Nano Letters* **2011,** *11* (3), 998-1001.
39. Chremos, A.; Theodorakis, P. E., Morphologies of Bottle-Brush Block Copolymers. *Acs Macro Letters* **2014,** *3* (10), 1096-1100.
40. Lee, J. Y.; Thompson, R. B.; Jasnow, D.; Balazs, A. C., Effect of nanoscopic particles on the mesophase structure of diblock copolymers. *Macromolecules* **2002,** *35* (13), 4855-4858.
41. Balazs, A. C.; Emrick, T.; Russell, T. P., Nanoparticle polymer composites: Where two small worlds meet. *Science* **2006,** *314* (5802), 1107-1110.
42. Yeh, S.-W.; Wei, K.-H.; Sun, Y.-S.; Jeng, U. S.; Liang, K. S., CdS Nanoparticles Induce a Morphological Transformation of Poly(styrene-b-4-vinylpyridine) from Hexagonally Packed Cylinders to a Lamellar Structure. *Macromolecules* **2005,** *38* (15), 6559-6565.
43. Smilgies, D. M., Scherrer grain-size analysis adapted to grazing-incidence scattering with area detectors. *J Appl Cryst, J Appl Crystallogr* **2009,** *42*, 1030-1034.
44. Jang, S. G.; Kramer, E. J.; Hawker, C. J., Controlled Supramolecular Assembly of Micelle-Like Gold Nanoparticles in PS-b-P2VP Diblock Copolymers via Hydrogen Bonding. *J. Am. Chem. Soc.* **2011,** *133* (42), 16986-16996.
45. Chiu, J. J.; Kim, B. J.; Kramer, E. J.; Pine, D. J., Control of nanoparticle location in block copolymers. *J. Am. Chem. Soc.* **2005,** *127* (14), 5036-5037.
46. Sides, S. W.; Kim, B. J.; Kramer, E. J.; Fredrickson, G. H., Hybrid particle-field simulations of polymer nanocomposites. *Phys Rev Lett* **2006,** *96* (25), -.
47. Jenczyk, J.; Woźniak-Budych, M.; Jancelewicz, M.; Jarek, M.; Jurga, S., Structural and dynamic study of block copolymer–Nanoparticles nanocomposites. *Polymer* **2019,** *167*, 130-137.